chemosensors

MDPI

Article

High-Performance Sulfur Dioxide Gas Sensor Based on Graphite-Phase Carbon-Nitride-Functionalized Tin Diselenide Nanorods Composite

Hao Zhang [1,2], Qiannan Pan [3], Yating Zhang [3], Yanting Zhang [1] and Dongzhi Zhang [3,*]

[1] College of Mechanical and Electrical Engineering, China University of Petroleum (East China), Qingdao 266580, China
[2] Technology Inspection Center, Shengli Oilfield, Dongying 257000, China
[3] College of Control Science and Engineering, China University of Petroleum (East China), Qingdao 266580, China
* Correspondence: dzzhang@upc.edu.cn

Abstract: In this paper, a composite of tin diselenide ($SnSe_2$) functionalized by graphite-phase carbon nitride (g-C_3N_4) was successfully prepared by a hydrothermal method, and was characterized by X-ray diffraction (XRD), scanning electron microscope (SEM) and X-ray photoelectron spectroscopy (XPS). These microstructure characterization results verified the successful synthesis of a multilayer g-C_3N_4/rod-shaped $SnSe_2$ composite. The gas sensitivity results showed that when the g-C_3N_4 ratio was 30%, the g-C_3N_4/$SnSe_2$ composite sensor had the highest response (28.9%) at 200 °C to 20 ppm sulfur dioxide (SO_2) gas, which was much higher than those of pristine g-C_3N_4 and $SnSe_2$ sensors at the optimum temperature. A series of comparative experiments proved that the g-C_3N_4/$SnSe_2$ composite sensor demonstrated an excellent response, strong reversibility and good selectivity for ppm-level SO_2 gas detection. The possible SO_2 sensing mechanism was ascribed to the heterostructure between the n-type $SnSe_2$ and n-type g-C_3N_4 nanomaterials. Furthermore, we also proposed the influence of the special structure of the g-C_3N_4 functionalized $SnSe_2$ composite on the gas-sensing characteristics.

Keywords: tin diselenide; carbon nitride; hydrothermal; heterostructure; SO_2 sensors

check for updates

Citation: Zhang, H.; Pan, Q.; Zhang, Y.; Zhang, Y.; Zhang, D. High-Performance Sulfur Dioxide Gas Sensor Based on Graphite-Phase Carbon-Nitride-Functionalized Tin Diselenide Nanorods Composite. *Chemosensors* **2022**, *10*, 401. https://doi.org/10.3390/chemosensors10100401

Academic Editor: Andrea Ponzoni

Received: 3 September 2022
Accepted: 2 October 2022
Published: 8 October 2022

Publisher's Note: MDPI stays neutral with regard to jurisdictional claims in published maps and institutional affiliations.

Copyright: © 2022 by the authors. Licensee MDPI, Basel, Switzerland. This article is an open access article distributed under the terms and conditions of the Creative Commons Attribution (CC BY) license (https://creativecommons.org/licenses/by/4.0/).

1. Introduction

As an important indicator of air pollution, sulfur dioxide (SO_2) is an irritating, highly toxic and colorless gas, which mainly comes from factory exhaust and automobile exhaust emissions [1,2]. When the emitted concentration of sulfur dioxide in air is too high, it is oxidized to sulfur trioxide and combined with water to form acid rain, which can destroy buildings, pollute the environment and reduce soil fertility [3,4]. In addition, human health is seriously threatened by some harmful gas species including sulfur dioxide gas. Respiratory diseases such as bronchitis and asthma can result from the excessive inhalation of sulfur dioxide gas [5]. There are reports that the human-permissible exposure limit for SO_2 gas is 5 ppm and the long-term exposure limit is 2 ppm [6]. Therefore, the development of portable, efficient and reliable gas sensors can be used to monitor the composition and concentration of environmental gas pollutants in the atmosphere, which can help people to deal with dangerous gases in time, and further protect social safety and human health.

Recently, two-dimensional (2D) layered inorganic materials (such as graphene and transition metal materials) have attracted attention due to their unique crystal structures and characteristics. Among them, two-dimensional transition metal dichalcogenides (TMDs) are ideal materials for preparing field effect transistors [7], photodetectors [8] and electronic devices [9] because of their unique electronic, magnetic, optical and mechanical properties. Due to their planar crystal structure, high specific surface area and

physical affinity, they also have unique advantages in sensing applications [10]. According to the reports from a few studies, two-dimensional transition metal compounds such as molybdenum disulfide (MoS_2) [11,12], tungsten disulfide (WS_2) [13,14] and tin diselenide ($SnSe_2$) [15,16] offer good gas sensing characteristics for detecting dangerous gases. $SnSe_2$ is an n-type two-dimensional transition chalcogenide, and its gas-sensitive properties have been widely reported [15–17]. The results of a study reported by Moreira et al. on the ammonia (NH_3) and nitrogen dioxide (NO_2) gas sensitivity of tin-diselenide-based sensors revealed that these sensors had steady repeatability and long-term stability under UV radiation [17]. Zhang et al. fabricated coral-like tin diselenide/metal-organic frameworks (MOFs)-derived nanoflower-like tin dioxide (SnO_2) heteronanostructures via a hydrothermal method. The $SnSe_2/SnO_2$ nanocomposite sensor exhibited excellent NO_2-sensing performance at room temperature, which was significantly improved under UV illumination. The enhanced NO_2 sensing performance was attributed to the formation of an n-n heterostructure and light-excited electrons [18]. By using the template-sacrificial approach, Wang et al. created rod-shaped $SnSe_2$ and polyhedral zinc oxide (ZnO) composite nanostructures, and the $ZnO/SnSe_2$ heterostructures exhibited an enhancement of carbon monoxide (CO)-sensing properties at room temperature [19]. Pan et al. reported a coral-like Au-modified $SnSe_2$ Schottky-junction-based ammonia gas sensor and demonstrated good gas sensitivity to ammonia gas detection. In addition, the effect of Au modification on ammonia gas molecules adsorption was also investigated using a first-principles density functional theory (DFT). Because of these studies, it can be concluded that $SnSe_2$ is a feasible material as building block for constructing high-performance gas sensors [20]. However, the use of a single $SnSe_2$ material for gas sensitivity research has certain limitations, and the test results may show poor selectivity and low sensitivity. According to previous studies, the sensing characteristics of gas sensors can be improved by forming a heterojunction [21,22]. Graphite-phase carbon nitride (g-C_3N_4), as a common two-dimensional material, has a structure like graphene and provides more active sites for gas adsorption. The material has excellent chemical stability, good electron mobility and low cost. In addition, g-C_3N_4 can also promote the uniform dispersion of active ingredients, so it can be used as a stable catalyst carrier [23,24].

In this paper, a composite of $SnSe_2$ functionalized by g-C_3N_4 was prepared via a hydrothermal method and served as the sensitive nanomaterial for SO_2 gas sensing. The nanostructure of the g-$C_3N_4/SnSe_2$ composite was characterized by X-ray diffraction (XRD), scanning electron microscope (SEM) and X-ray photoelectron spectroscopy (XPS). The characterization results verified the successful synthesis of a multilayer g-C_3N_4/rod-shaped $SnSe_2$ composite. The as-prepared g-$C_3N_4/SnSe_2$ composite sensor showed an excellent gas response and rapid adsorption/desorption ability towards SO_2 under the optimal temperature of 200 °C, which was much higher than those of pristine g-C_3N_4 and $SnSe_2$ sensors. A series of comparative experiments proved that the g-$C_3N_4/SnSe_2$ composite sensor demonstrated an excellent response, strong reversibility and good selectivity for ppm-level SO_2 gas detection. In this paper, two innovative two-dimensional materials, g-C_3N_4 and $SnSe_2$, were used to discuss in detail the mechanisms that may improve the SO_2 sensing performance, such as the synergistic interaction between g-C_3N_4 and $SnSe_2$, and the effective structural features.

2. Experimental Section

2.1. Materials

Tin chloride dihydrate ($SnCl_2{\cdot}2H_2O$), hydrazine hydrate ($N_2H_4{\cdot}H_2O$), selenium dioxide (SeO_2), ethanol (CH_3CH_2OH) and graphitic carbon nitride (g-C_3N_4) were all supplied by Sinopharm Chemical Reagent Co. Ltd. (Shanghai, China).

2.2. Material Synthesis and Sensor Fabrication

The preparation process of the materials is shown in Figure 1. The $SnSe_2$ was prepared by a hydrothermal reduction method. A total of 0.01 mol $SnCl_2{\cdot}2H_2O$ and 0.02 mol SeO_2

were added into 70 mL deionized water and stirred for 30 min. A total of 10 mL of hydrazine hydrate was added into the above mixture solution, and then transferred to a 100 mL Teflon-lined stainless-steel autoclave, and hydrothermally treated at 180 °C for 24 h. The resulting precipitate was filtered, washed and dried at 60 °C for 8 h to obtain a black tin diselenide product.

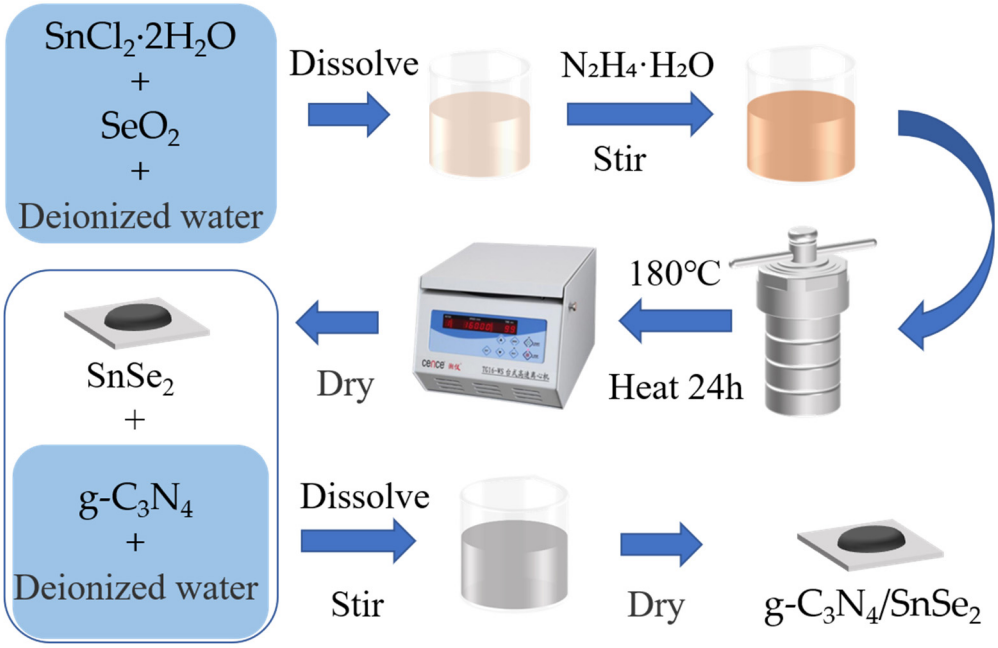

Figure 1. Synthesis process of g-C_3N_4/$SnSe_2$ nanomaterials.

A total of 280 mg of $SnSe_2$ powder and 120 mg of g-C_3N_4 powder were dissolved in 20 mL of DI water. After vigorously stirring for 1 h, the g-C_3N_4 was effectively anchored on the surface of $SnSe_2$. The resulting product was dried at 60 °C for overnight. Finally, the g-C_3N_4/$SnSe_2$ composite was obtained. The composite materials with different ratios (0, 20, 30, and 50%) of g-C_3N_4 and $SnSe_2$ were prepared by adjusting the quality ratio of g-C_3N_4 and $SnSe_2$. In addition, the two materials were dispersed in deionized water in a certain proportion, and after a period of ultrasonic treatment, they were effectively combined through strong physical effects and interactions between charges.

2.3. Gas Sensor Fabrication

The structure illustration of the ceramic tube based SO_2 gas sensor is shown in Figure 2. It consisted of an Al_2O_3 ceramic tube and a base. The ceramic tube was 4 mm long and 1.2 mm in diameter, and its surface was equipped with gold electrodes and two pairs of platinum wires for electrical signals. The heating resistor of the Ni–Cr alloy coil passed through a hollow ceramic tube for heating. The sensing layer materials were coated on the surface of the ceramic tube, and the electrodes were led out to complete the preparation of the sensor. After preparing the sensing film, the sensor was dried at 60 °C for 6 h and then aged at 200 °C for 24 h before the test to obtain good resistance stability. The SO_2-sensing measurement was performed in a home-made gas sensing detection system [25] as shown in Figure 3. The sensor was placed in a home-made chamber, and the SO_2 gas with different concentrations of 1–200 ppm was obtained by diluting 1000 ppm SO_2 standard gas with high-purity air. The sensor resistance was measured with an Agilent 34970A digital multimeter and connected with a computer through RS-232 for data acquisition. The operation temperature of the sensor was controlled by an applied voltage to the Ni–Cr heating resistor. A steady power supply of GPD-4303S was employed for applying voltage for heating. The response of the sensor is defined as $S = (R_A - R_G)/R_A \times 100\%$ (R_A: resistance in air; R_G: resistance in SO_2 gas).

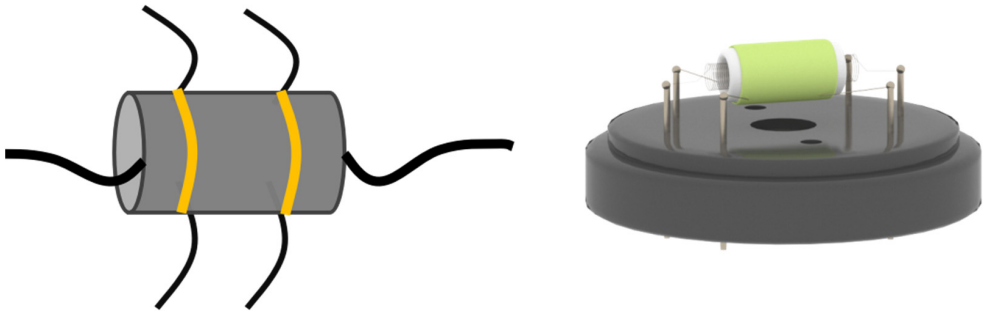

Figure 2. Structure illustration of the ceramic-tube-based SO_2 gas sensor.

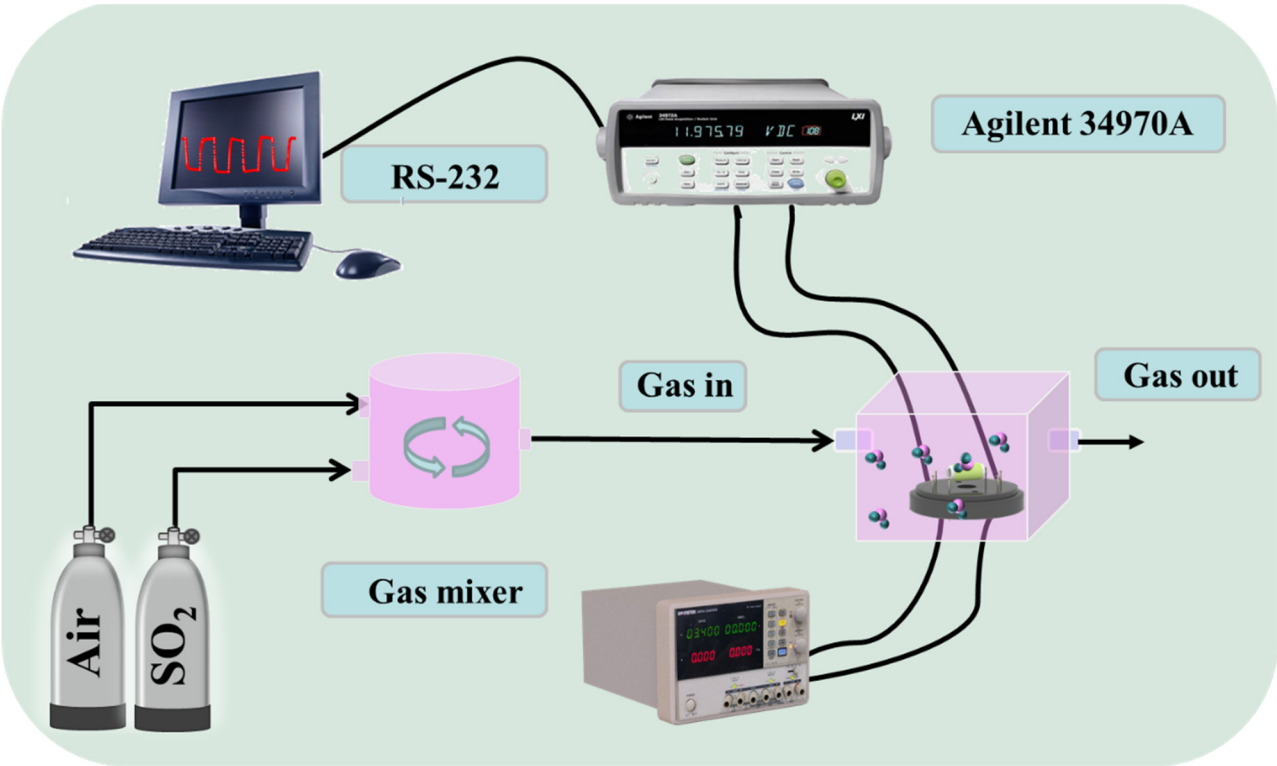

Figure 3. Schematic illustration of sensor performance test platform.

3. Results and Discussion

3.1. Structure Characterization

The crystal structures of the $SnSe_2$, g-C_3N_4 and g-C_3N_4/$SnSe_2$ were characterized by X-ray powder diffraction (XRD, Rigaku D/Max-2550, Rigaku, Japan) with Cu Kα radiation (λ = 0.15418 nm). X-ray photoelectron spectroscopy (XPS, Thermo Scientific K-Alpha XPS spectrometer, Thermo Scientific, Waltham, MA, USA) was used to detect the chemical composition of the samples, and the morphology of pristine $SnSe_2$, g-C_3N_4 and g-C_3N_4/$SnSe_2$ nanocomposites were observed by a scanning electron microscope (SEM, Hitachi S-4800, Hitachi, Japan). The g-C_3N_4/$SnSe_2$ sample with a ratio of 30% g-C_3N_4 was used for characterization.

The crystal phases of the as-prepared materials were identified by XRD analysis. As shown in Figure 4a, the peaks of $SnSe_2$ (JCPDS card number 23-0602) located at 14.38°, 26.98°, 30.88°, 40.17°, 47.77°, 50.19°, 52.58°, 57.92°, 60.34°, 63.96° and 78.22° corresponded to the (001), (100), (011), (012), (110), (111), (103), (201), (004), (202) and (121) diffraction planes of the orthorhombic-phase $SnSe_2$ structures, respectively [26]. The XRD pattern of g-C_3N_4 was well in accordance with the hexagonal crystal g-C_3N_4 (JCPDS Card no. 36-1451) [27]. The formation of the two diffraction peaks of (100) and (002) can be attributed

to the in-plane structure stacking of the tri-s-triazine part and the in-plane stacking of the conjugated aromatic hydrocarbon system, respectively. There were corresponding characteristic peaks of g-C_3N_4 and $SnSe_2$ in the XRD pattern of the g-C_3N_4/$SnSe_2$ nanocomposite, and there were no other characteristic peaks, indicating the successful preparation of the $SnSe_2$/g-C_3N_4 composite.

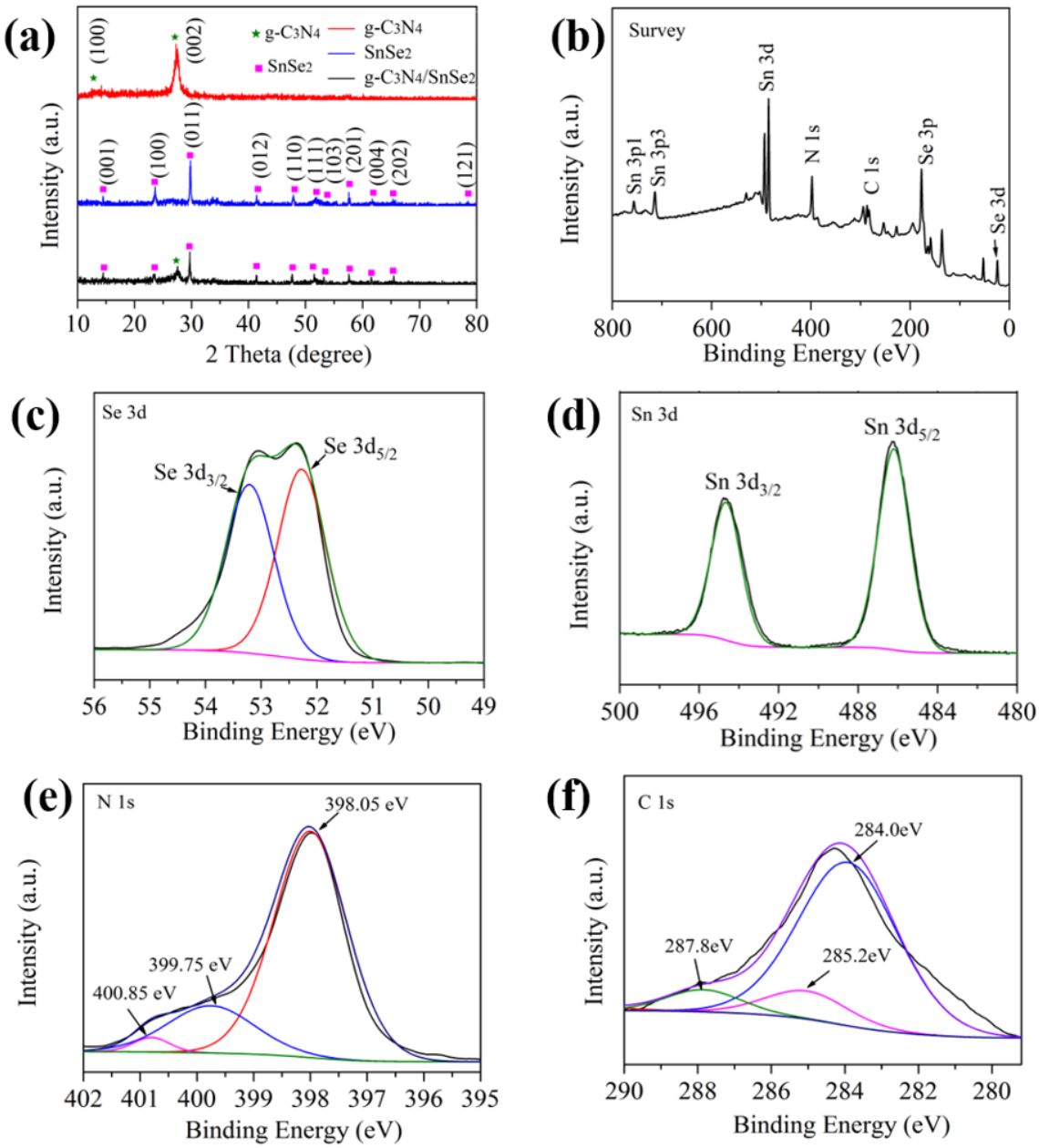

Figure 4. (**a**) XRD patterns of g-C_3N_4, $SnSe_2$ and g-C_3N_4/$SnSe_2$. XPS spectra of g-C_3N_4/$SnSe_2$ product: (**b**) full spectrum, (**c**) Se 3d, (**d**) Sn 3d, (**e**) N 1s and (**f**) C 1s.

XPS is a measurement technique for detecting the elemental composition and chemical valence of materials. Figure 4b is the total spectrum of the g-C_3N_4/$SnSe_2$ composite, and the existence of the four elements Se, Sn, C and N was confirmed from the peak positions in the figure. The Se 3D spectrum shown in Figure 4c is represented by two peaks with binding energies of 53.4 and 52.2 eV, corresponding to Se $3d_{5/2}$ and Se $3d_{3/2}$, respectively [28–30]. The Sn 3d spectrum shown in Figure 4d shows two distinctive peaks at energies of 486.3 and 495.2 eV, which correspond to Sn $3d_{5/2}$ and $3d_{3/2}$, respectively.

Since there was an energy difference of 8.4 eV between the two peaks, the Sn^{4+} state can be confirmed [31]. Figure 4e is the characteristic peak of N 1s. Three asymmetric peaks at 398.3, 400.0 and 401.0 eV were attributed to C=N-C, N-$(C)_3$ and C-N-H, respectively. Figure 4f shows the XPS spectrum of C 1s, where the characteristic peak at 284.6 eV was due to the formation of indefinite carbon absorption on the surface of the material, and the diffraction peak at 287.8 eV may be formed by N=C-N coordination [32].

SEM is a detection technology used to observe the micro-morphology of nanomaterials. Figure 5 shows the SEM characterization of the g-C_3N_4/$SnSe_2$-sensitive material. Figure 5a shows the SEM characterization of the intrinsic $SnSe_2$. The $SnSe_2$ nanorods were composed of numerous nanoparticles, the cross-sectional radius and the length of which were about 300−500 nm and 3−5 µm, respectively. Figure 5b shows the SEM characterization image of the graphite-like-phase carbon nitride. The exfoliated g-C_3N_4 nanosheets had a 2D layered morphology, which was manifested as multiple thin layers stacking together. Figure 5c,d show the surface morphology of the g-C_3N_4/$SnSe_2$ composite. It can be clearly observed that the nanorod-shaped $SnSe_2$ and multilayer g-C_3N_4 grew and aggregated together well, which show s that the g-C_3N_4/$SnSe_2$ composite was successfully synthesized.

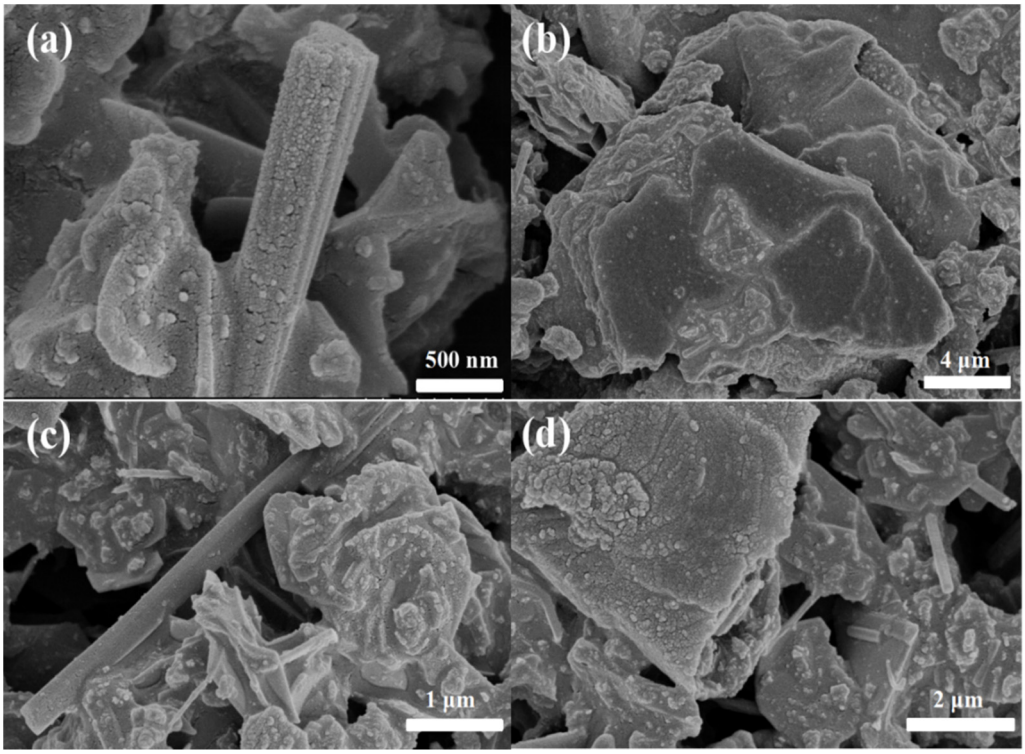

Figure 5. SEM images of (**a**) $SnSe_2$, (**b**) g-C_3N_4, and (**c**,**d**) g-C_3N_4/$SnSe_2$.

3.2. SO_2-Sensing Properties

The working temperature is an important key variable related to the sensing characteristics of the g-C_3N_4/$SnSe_2$ sensor [33–35]. It affects the chemical adsorption and surface reaction of gas molecules. Therefore, to determine the optimal operating temperature as well as the optimum ratio of the two materials, we studied the responses of pristine g-C_3N_4, pristine $SnSe_2$ and the x% g-C_3N_4/$SnSe_2$ (x = 0, 20, 30, 50) film sensors to 20 ppm SO_2 gas at different operating temperatures. As shown in Figure 6a, the operating temperatures and responses of the sensors presented a "triangular" shape. The optimal temperatures of g-C_3N_4, $SnSe_2$ and g-C_3N_4/$SnSe_2$ were 250 °C, 200 °C and 200 °C, respectively. When the g-C_3N_4 ratio was 30%, the response (28.9%) of g-C_3N_4/$SnSe_2$ at 200 °C was the highest, which was much higher than those of the pristine g-C_3N_4 and $SnSe_2$. The gas-sensing properties of the $SnSe_2$, g-C_3N_4 and 30% g-C_3N_4/$SnSe_2$ sensors

were investigated by recording the changes in resistance when they were exposed to different concentrations (1−200 ppm) of SO_2 gas at 200 °C, as shown in Figure 6b. When switched to air, the resistances of the three sensors returned to the base value in air. The response values of 30% g-C_3N_4/$SnSe_2$ towards 1, 5, 10, 20, 50, 100, 200 ppm SO_2 gas were, respectively, 8.82%, 15.59%, 20.22%, 28.52%, 35.09%, 41.54% and 44.34%, higher than those of the pristine $SnSe_2$ and g-C_3N_4. Figure 6c shows the fitting curves of the three sensors between sensitivity (Y) and concentration of SO_2 (X). The fitting functions of g-C_3N_4, $SnSe_2$ and g-C_3N_4/$SnSe_2$ sensors were $Y = 14.89 - 11.82 \times 0.98^X$, $Y = 22.76 - 17.85 \times 0.95^X$ and $Y = 42.16 - 33.15 \times 0.96^X$, respectively. The R^2 of the fitting curve of the g-C_3N_4/$SnSe_2$ sensor was 0.975. Figure 6d shows the response/recovery curves of the g-C_3N_4/$SnSe_2$ sensor toward the desired concentrations of SO_2 gas. The sensor exhibited stable response and recovery behaviors.

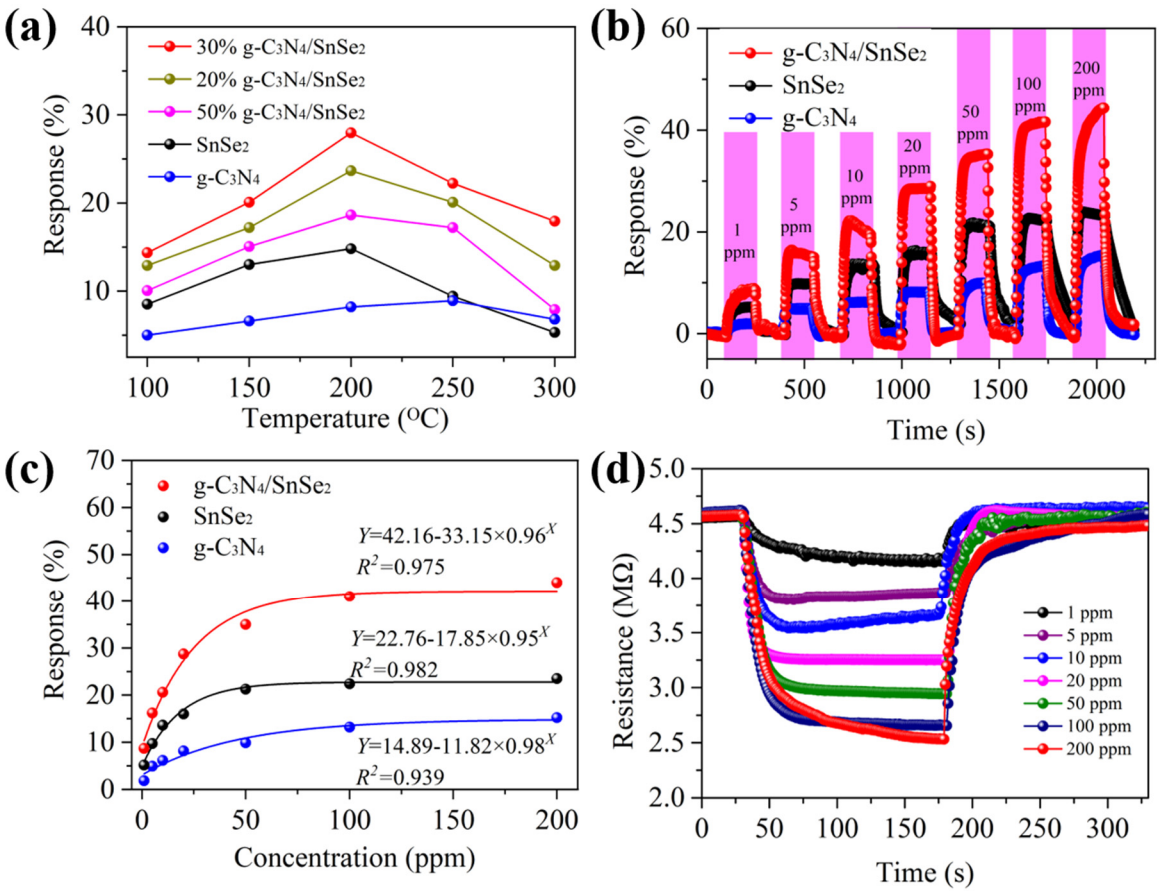

Figure 6. (**a**) Responses of g-C_3N_4/$SnSe_2$ composites with different quality ratios to 20 ppm SO_2 gas at various temperatures. (**b**) Sensing properties of pristine g-C_3N_4, $SnSe_2$ and g-C_3N_4/$SnSe_2$ composite sensors at different concentrations of SO_2 gas at 200 °C. (**c**) Response fitting curves of three sensors versus SO_2 concentration at 200 °C. (**d**) Typical response–recovery curves for various concentrations of SO_2 gas at 200 °C.

The repeatability of the g-C_3N_4/$SnSe_2$ composite sensor against a gas with a concentration of 50 ppm SO_2 at 200 °C is examined in Figure 7a. For each run, the resistance could fully recover its initial state and changes from 4.5 MΩ to 2.9 MΩ, showing a good reproducibility. Figure 7b shows the response/recovery curves of the g-C_3N_4, $SnSe_2$, and g-C_3N_4/$SnSe_2$ composite sensors exposed to 50 ppm SO_2 gas. The response/recovery time of the g-C_3N_4/$SnSe_2$ sensor was 22/24 s, while the values of the pristine g-C_3N_4 and $SnSe_2$ sensors were 46/55 s and 26/82 s, respectively, suggesting that the g-C_3N_4/$SnSe_2$ sensor had a faster detection rate towards SO_2 gas compared with the pristine g-C_3N_4 and $SnSe_2$ sensors at 200 °C. Excellent selectivity is also an important factor for nanomaterial-based

gas sensors [36,37]. Therefore, we further studied the SO_2 selectivity of the g-C_3N_4/$SnSe_2$ composite sensor at 200 °C. The sensor was exposed to 50 ppm of various interfering gases, such as LPG, CO, CH_4, H_2S and H_2. As shown in Figure 7c, the g-C_3N_4/$SnSe_2$ composite sensor had the highest response to SO_2 gas, indicating that the selectivity to SO_2 gas was excellent. Additionally, the long-term stability of the g-C_3N_4/$SnSe_2$ composite sensor for various SO_2 gas concentrations (1, 10 and 50 ppm) at a working temperature of 200 °C was examined. The sensor's response had no obvious changes in a period under the same experimental conditions and exhibited a good stability, as shown in Figure 7d.

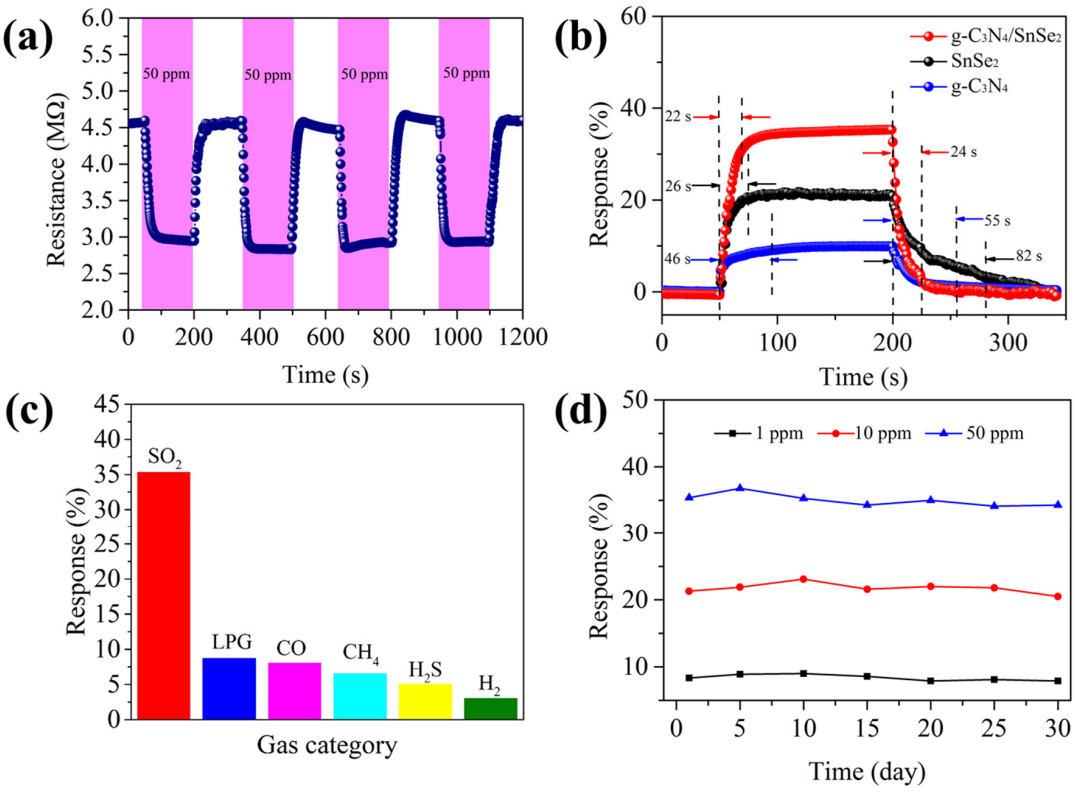

Figure 7. At the optimal temperature of 200 °C (**a**) repeatability of g-C_3N_4/$SnSe_2$ composite sensor. (**b**) Response/recovery curves of g-C_3N_4, $SnSe_2$ and g-C_3N_4/$SnSe_2$ composite sensors exposed to 50 ppm SO_2 gas. (**c**) Selectivity and (**d**) long-term stability of g-C_3N_4/$SnSe_2$ composite sensor.

Numerous studies have described the detection of SO_2 gases utilizing a variety of sensitive materials up to this point. As far as we know, there have been no studies using g-C_3N_4/$SnSe_2$ for SO_2 gas detection. Table 1 lists the comparison of this work with previously reported works. The different SO_2 gas sensors are compared in terms of sensing environment, response value and gas concentration. The comparison results showed that the as-prepared g-C_3N_4/$SnSe_2$ sensor featured a higher response value and a lower operating temperature.

Table 1. Comparison of the SO_2-sensing performance between the present work and previous reported studies.

Sensing Material	Sensing Environment	Response	Concentration	Ref.
AlGaN/ZnO/rGO	RT	2.5%	120 ppb	[38]
SnO_2/rGO	RT/UV	1.7%	5 ppm	[39]
Pt/rGO	120 °C	5%	100 ppm	[40]
g-C_3N_4/rGO	RT	3.2%	100 ppm	[41]
SnO_2/MWCNT	60 °C	6	500 ppm	[42]

Table 1. *Cont.*

Sensing Material	Sensing Environment	Response	Concentration	Ref.
$V_2O_5/WO_3/TiO_2$	400 °C	5%	20 ppm	[43]
WO_3	350 °C	5%	1 ppm	[44]
Cu–SnO_2	400 °C	1.1%	20 ppm	[45]
SnO_2–PANI	RT	3.1%	4 ppm	[46]
TiO_2/rGO	RT	11.14%	5 ppm	[47]
NiO–SnO_2	180 °C	8.3%	50 ppm	[48]
TiO_2	200 °C	11%	10 ppm	[49]
ZnO	RT	0.2%	100 ppm	[50]
WO_3–PANI	RT	4.3%	5 ppm	[51]
Ni–MoS_2	RT	7.4%	5 ppm	[52]
V_2O_5/SnO_2	350 °C	45%	5 ppm	[53]
V-doped TiO_2	400 °C	10%	10 ppm	[54]
GO	RT	6%	5 ppm	[55]
PANI	RT	4.2%	10 ppm	[56]
g-$C_3N_4/SnSe_2$	200 °C	28.9%	20 ppm	This work

3.3. SO_2 Gas-Sensing Mechanism

The sensing mechanism has been widely explained using the surface charge caused by adsorbed oxygen. For the pristine $SnSe_2$ gas sensor, when exposed to air, oxygen molecules in air adsorb on the surface of the sensing material to form adsorbed oxygen molecules. The adsorbed oxygen molecules extract electrons from the conduction band of $SnSe_2$ to form chemically adsorbed oxygen O^- at 200 °C. On the surface of the g-$C_3N_4/SnSe_2$ sensing material, an electron depletion layer consequently forms. The following is a description of the reactions [57,58]:

$$O_2\ (gas) \rightarrow O_2\ (ads) \quad (1)$$

$$O_2\ (ads) + 2e^- \rightarrow 2O^-\ (ads) \quad (2)$$

When the reducing gas SO_2 is introduced, the SO_2 molecules adsorbed on the surface of the sensing material will further react with O^- ions and release electrons to the $SnSe_2$ conduction band to form SO_3, thereby increasing the number of charge carriers and reducing the resistance of the sensor. The specific reaction process is illustrated as follows [59]:

$$SO_2\ (ads) + O^-\ (ads) \rightarrow SO_3 + e^- \quad (3)$$

In our experiment, it is worth noting that the g-$C_3N_4/SnSe_2$ sensor exhibited an improved response to SO_2 gas than the pristine C_3N_4 and $SnSe_2$ sensors. This phenomenon could be explained by two positive factors of g-C_3N_4 decoration. Firstly, the morphology, specific surface area and electrical properties of the material are important factors affecting its gas-sensing performance [60]. The addition of the layered two-dimensional structure of g-C_3N_4 increases the specific surface area of the composite material and provides more active sites, increasing the production of adsorbed oxygen. Another factor influencing the effectiveness of the gas sensing system is the n-n heterojunction created between g-C_3N_4 and $SnSe_2$ [61–63]. Figure 8a shows the energy band structure of the heterojunction formed by the n-type $SnSe_2$ nanorods and n-type g-C_3N_4 layered nanosheets in air, where the band gaps of $SnSe_2$ and g-C_3N_4 were 1.37 and 2.7 eV, respectively. Their Fermi levels were different, and the work function (4.3 eV) of $SnSe_2$ was lower than that (4.67 eV) of g-C_3N_4 [64]. When the two materials contact with different work functions, electrons will transfer from $SnSe_2$ to g-C_3N_4 to reach a Fermi energy balance. Therefore, the n-n heterojunction is formed at the interface between $SnSe_2$ and g-C_3N_4 in air [65]. When exposed to SO_2 gas, SO_2 molecules absorbed on the surface of the composite material react with O^- to generate electrons [66]. Therefore, the carrier concentration in the heterojunction increases by receiving electrons, resulting in a narrowing of the depletion layer at the interface of the two materials [61,67,68], which reduces the resistance of the sensor (Figure 8b). The built-

in electric field generated by the nano-scale heterojunction can accelerate the separation process of electrons and facilitate electron transfer.

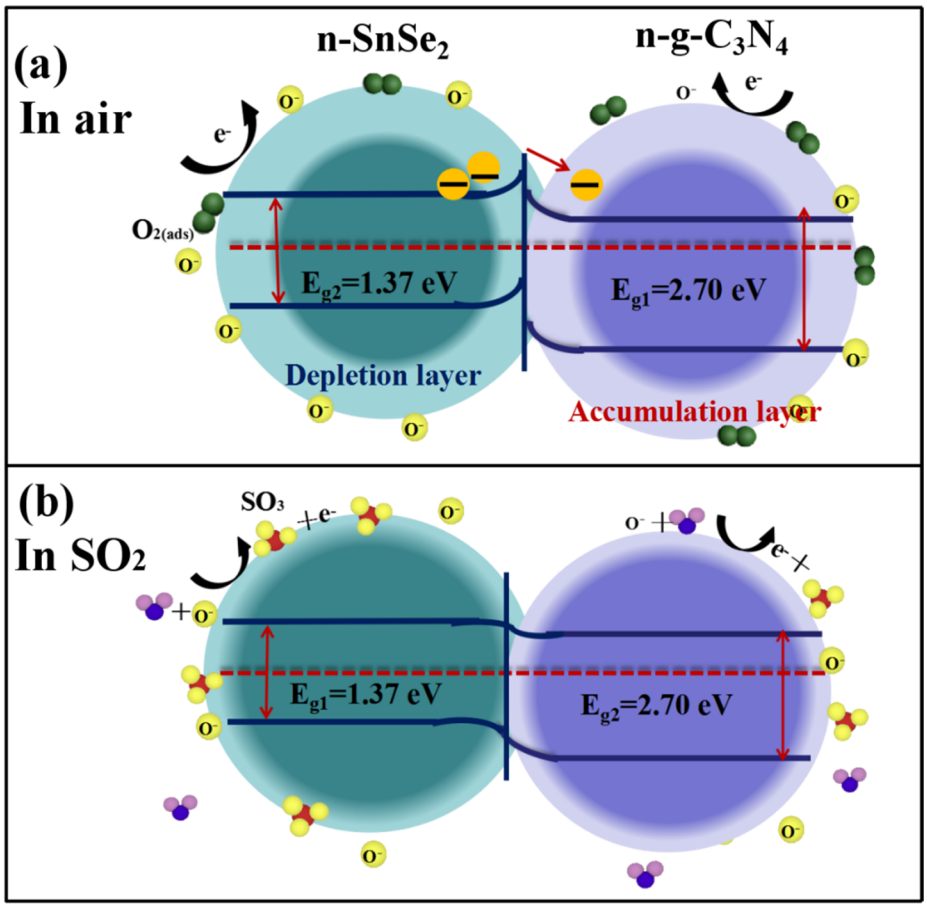

Figure 8. Schematic diagram of microscopic sensing mechanism of g-C_3N_4/$SnSe_2$ composite sensor.

4. Conclusions

In this paper, a g-C_3N_4 functionalized $SnSe_2$ composite thin film sensor was successfully prepared. XRD, XPS and SEM techniques were used to characterize the elements and structure of the g-C_3N_4/$SnSe_2$ composite material. The optimal temperature (200 °C) of the g-C_3N_4/$SnSe_2$ composite sensor was determined through gas-sensing experiments under different working temperatures. The SO_2 gas-sensing performance for the g-C_3N_4/$SnSe_2$ composite sensor was investigated at the optimal temperature. The experimental results showed that under the optimal temperature, the 30% g-C_3N_4/$SnSe_2$ composite sensor gained the highest sensitivity to SO_2 gas. The two-dimensional layered structure of the g-C_3N_4-modified n-type $SnSe_2$ nanorods not only increased the specific surface area and the gas adsorption site of the g-C_3N_4/$SnSe_2$ sensor, but also formed an n-n heterojunction between the g-C_3N_4 nanosheets and $SnSe_2$ nanorods, which improved the sensing performance of the g-C_3N_4/$SnSe_2$ sensor toward SO_2 gas.

Author Contributions: Conceptualization, H.Z. and Q.P.; methodology, D.Z.; validation, H.Z. and Q.P.; formal analysis, H.Z. and Q.P.; investigation, Y.Z. (Yanting Zhang); data curation, H.Z. and Q.P.; writing—original draft preparation, Q.P.; writing—review and editing, Y.Z. (Yating Zhang) and D.Z.; visualization, Q.P. and Y.Z. (Yating Zhang); supervision, D.Z.; funding acquisition, D.Z. All authors have read and agreed to the published version of the manuscript.

Funding: This research was funded by the Original Innovation Special Project of Science and Technology Plan of Qingdao West Coast New Area, China (2020-85).

Institutional Review Board Statement: Not applicable.

Informed Consent Statement: Not applicable.

Data Availability Statement: Not applicable.

Conflicts of Interest: The authors declare no conflict of interest.

References

1. Das, S.; Rana, S.; Mursalin, S.; Rana, P.; Sen, A. Sonochemically prepared nanosized $BiFeO_3$ as novel SO_2 sensor. *Sens. Actuators B* **2015**, *218*, 122–127. [CrossRef]
2. Jung, G.; Jeong, Y.; Hong, Y.; Wu, M.; Hong, S.; Shin, W.; Park, J.; Jang, D.; Lee, J. SO_2 gas sensing characteristics of FET- and resistor-type gas sensors having WO_3 as sensing material. *Solid-State Electron.* **2020**, *165*, 107747. [CrossRef]
3. Ma, C.; Hao, X.; Yang, X.; Liang, X.; Liu, F.; Liu, T.; Yang, C.; Zhu, H.; Lu, G. Sub-ppb SO_2 gas sensor based on NASICON and $La_xSm_{1-x}FeO_3$ sensing electrode. *Sens. Actuators B Chem.* **2018**, *256*, 648–655. [CrossRef]
4. Liu, L.; Liu, S. Oxygen vacancies as an efficient strategy for promotion of low concentration SO_2 gas sensing: The case of Au-modified SnO_2. *ACS Sustain. Chem. Eng.* **2018**, *6*, 13427–13434. [CrossRef]
5. Liu, F.; Wang, J.; Jiang, L.; You, R.; Wang, Q.; Wang, C.; Lin, Z.; Yang, Z.; He, J.; Liu, A.; et al. Compact and planar type rapid response ppb-level SO_2 sensor based on stabilized zirconia and $SrMoO_4$ sensing electrode. *Sens. Actuators B Chem.* **2020**, *307*, 127655. [CrossRef]
6. Tong, P.; Hoa, N.; Nha, H.; Duy, N.; Hung, C.; Hieu, N. SO_2 and H_2S sensing properties of hydrothermally synthesized CuO nanoplates. *J. Electron. Mater.* **2018**, *47*, 7170–7178. [CrossRef]
7. Goel, N.; Kumar, R.; Jain, S.; Rajamani, S.; Roul, B.; Gupta, G.; Kumar, M.; Krupanidhi, S. A high-performance hydrogen sensor based on a reverse-biased MoS_2/GaN heterojunction. *Nanotechnology* **2019**, *30*, 314001. [CrossRef]
8. Xu, T.; Han, Y.; Lin, L.; Xu, J.; Fu, Q.; He, H.; Song, B.; Gai, Q.; Wang, X. Self-power position-sensitive detector with fast optical relaxation time and large position sensitivity basing on the lateral photovoltaic effect in tin diselenide films. *J. Alloys Compd.* **2019**, *790*, 941–946. [CrossRef]
9. Javed, Y.; Mirza, S.; Li, C.; Xu, X.; Rafiq, M. The role of biaxial strain and pressure on the thermoelectric performance of $SnSe_2$: A first principles study. *Semicond. Sci. Technol.* **2019**, *34*, 055009. [CrossRef]
10. Gu, D.; Wang, X.; Liu, W.; Li, X.; Lin, S.; Wang, J.; Rumyantseva, M.; Gaskovc, A.; Akbar, S. Visible-light activated room temperature NO_2 sensing of SnS_2 nanosheets based chemiresistive sensors. *Sens. Actuators B Chem.* **2020**, *305*, 127455. [CrossRef]
11. Jaiswal, J.; Sanger, A.; Tiwari, P.; Chandra, R. MoS_2 hybrid heterostructure thin film decorated with CdTe quantum dots for room temperature NO_2 gas sensor. *Sens. Actuators B Chem.* **2020**, *305*, 127437. [CrossRef]
12. Shen, J.; Yanga, Z.; Wang, Y.; Xu, L.; Liu, R.; Liu, X. The gas sensing performance of borophene/MoS_2 heterostructure. *Appl. Surf. Sci.* **2020**, *504*, 144412. [CrossRef]
13. Liu, D.; Tang, Z.; Zhang, Z. Comparative study on NO_2 and H_2S sensing mechanisms of gas sensors based on WS_2 nanosheets. *Sens. Actuators B Chem.* **2020**, *303*, 127114. [CrossRef]
14. Zhou, Q.; Zhu, L.; Zheng, C.; Wang, J. Nanoporous Functionalized WS2/MWCNTs Nanocomposite for Trimethylamine Detection Based on Quartz Crystal Microbalance Gas Sensor. *ACS Appl. Mater. Interfaces* **2021**, *13*, 41339–41350. [CrossRef] [PubMed]
15. Pawar, M.; Kadam, S.; Late, D. High-performance sensing behavior using electronic ink of 2D $SnSe_2$ nanosheets. *Chem. Sel.* **2017**, *2*, 4068–4075. [CrossRef]
16. Wang, X.; Liu, Y.; Dai, J.; Chen, Q.; Huang, X.; Huang, W. Solution-processed p-SnSe/n-$SnSe_2$ hetero-structure layers for ultrasensitive NO_2 detection. *Chem. Eur. J.* **2020**, *26*, 3870–3876. [CrossRef]
17. Moreira, O.; Cheng, W.; Fuh, H.; Chien, W.; Yan, W.; Fei, H.; Xu, H.; Zhang, D.; Chen, Y.; Zhao, Y.; et al. High Selectivity Gas Sensing and Charge Transfer of $SnSe_2$. *ACS Sens.* **2019**, *4*, 2546–2552. [CrossRef] [PubMed]
18. Li, T.; Zhang, D.; Pan, Q.; Tang, M.; Yu, S. UV enhanced NO_2 gas sensing at room temperature based on coral-like tin diselenide/MOFs-derived nanoflower-like tin dioxide heteronanostructures. *Sens. Actuators B Chem.* **2022**, *355*, 131049. [CrossRef]
19. Wang, D.; Zhang, D.; Pan, Q.; Wang, T.; Chen, F. Gas sensing performance of carbon monoxide sensor based on rod-shaped tin diselenide/MOFs derived zinc oxide polyhedron at room temperature. *Sens. Actuators B Chem.* **2022**, *371*, 132481. [CrossRef]
20. Pan, Q.; Li, T.; Zhang, D. Ammonia gas sensing properties and density functional theory investigation of coral-like Au-$SnSe_2$ Schottky junction. *Sens. Actuators B Chem.* **2021**, *332*, 129440. [CrossRef]
21. Sun, K.; Zhan, G.; Chen, H.; Lin, S. Low-Operating-Temperature NO_2 Sensor Based on a CeO_2/ZnO Heterojunction. *Sensors* **2022**, *21*, 8269. [CrossRef] [PubMed]
22. Liu, K.; Liu, H.; Wang, J.; Feng, L. Synthesis and characterization of $SnSe_2$ hexagonal nanoflakes. *Mater. Lett.* **2009**, *63*, 512–514. [CrossRef]
23. David, S.P.S.; Veeralakshmi, S.; Priya, M.S.; Nehru, S.; Kalaiselvam, S. Room-temperature chemiresistive g-C_3N_4/Ag_2ZrO_3 nanocomposite gas sensor for ethanol detection. *J. Mater. Sci.-Mater. El.* **2022**, *33*, 11498–11510. [CrossRef]
24. Pan, W.; Zhang, Y.; Yu, S.; Liu, X.; Zhang, D. Hydrogen sulfide gas sensing properties of metal organic framework-derived α-Fe_2O_3 hollow nanospheres decorated with $MoSe_2$ nanoflowers. *Sens. Actuators B Chem.* **2021**, *344*, 130221. [CrossRef]
25. Yang, Z.; Zhang, D.; Chen, H. MOF-derived indium oxide hollow microtubes/MoS_2 nanoparticles for NO_2 gas sensing. *Sens. Actuators B Chem.* **2019**, *300*, 127037. [CrossRef]

26. Liu, C.; Huang, Z.; Wang, D.; Wang, X.; Miao, L.; Wang, X.; Wu, S.; Toyama, N.; Asaka, T.; Chen, J.; et al. Dynamic Ag^+-intercalation with $AgSnSe_2$ nanoprecipitates in Cl-doped polycrystalline $SnSe_2$ toward ultra-high thermoelectric performance. *J. Mater. Chem. A* **2019**, *7*, 9761–9772. [CrossRef]
27. Hang, N.; Zhang, S.; Yang, W. Efficient exfoliation of g-C_3N_4 and NO_2 sensing behavior of graphene/g-C_3N_4 nanocomposite. *Sens. Actuators B Chem.* **2017**, *248*, 940–948. [CrossRef]
28. Zhang, D.; Yang, Z.; Li, P.; Pang, M.; Xue, Q. Flexible self-powered high-performance ammonia sensor based on Au-decorated $MoSe_2$ nanoflowers driven by single layer MoS_2-flake piezoelectric nanogenerator. *Nano Energy* **2019**, *65*, 103974. [CrossRef]
29. Yan, J.; Song, Z.; Xu, H.; Lee, L. Carbon-mediated electron transfer channel between SnO_2 QDs and g-C_3N_4 for enhanced photocatalytic H_2 production. *Chem. Eng. J.* **2021**, *425*, 131512. [CrossRef]
30. Yan, J.; Wang, T.; Qiu, S.; Song, Z.; Zhu, W.; Liu, X.; Liang, J.; Sun, C.; Li, H. Insights into the efficient charge separation over Nb_2O_5/2D-C_3N_4 heterostructure for exceptional visible-light driven H_2 evolution. *J. Energy Chem.* **2022**, *65*, 548–555. [CrossRef]
31. Xiong, Y.; Lu, W.; Ding, D.; Zhu, L.; Li, X.; Ling, C.; Xue, Q. Enhanced room temperature oxygen sensing properties of LaOCl-SnO_2 hollow spheres by UV light illumination. *ACS Sens.* **2017**, *2*, 679–686. [CrossRef] [PubMed]
32. Zeng, B.; Zhang, L.; Wan, X. Fabrication of α-Fe_2O_3/g-C_3N_4 composites for cataluminescence sensing of H_2S. *Sens. Actuators B Chem.* **2015**, *211*, 370–376. [CrossRef]
33. Guo, J.; Zhang, J.; Zhu, M.; Ju, D.; Xu, H.; Cao, B. High-performance gas sensor based on ZnO nanowires functionalized by Au nanoparticles. *Sens. Actuator B* **2014**, *199*, 339–345. [CrossRef]
34. Zhou, X.; Feng, W.; Wang, C.; Hu, X.; Li, X.; Sun, P.; Shimanoe, K.; Yamazoe, N.; Lu, G. Porous ZnO/$ZnCo_2O_4$ hollow spheres: Synthesis, characterization, and applications in gas sensing. *J. Mater. Chem. A* **2014**, *2*, 17683–17690. [CrossRef]
35. Bai, S.; Chen, C.; Luo, R.; Chen, A.; Li, D. Synthesis of MoO_3/reduced graphene oxide hybrids and mechanism of enhancing H_2S sensing performances. *Sens. Actuator B* **2015**, *216*, 113–120. [CrossRef]
36. Zhang, D.; Cao, Y.; Wu, J.; Zhang, X. Tungsten trioxide nanoparticles decorated tungsten disulfide nanoheterojunction for highly sensitive ethanol gas sensing application. *Appl. Surf. Sci.* **2020**, *503*, 144063. [CrossRef]
37. Zhang, D.; Yang, Z.; Yu, S.; Mi, Q.; Pan, Q. Diversiform metal oxide-based hybrid nanostructure for gas sensing with versatile prospects. *Coord. Chem. Rev.* **2020**, *413*, 213272. [CrossRef]
38. Triet, N.M.; Duy, L.T.; Hwang, B.U.; Hanif, A.; Siddiqui, S.; Park, K.H.; Cho, C.Y.; Lee, N.E. High-performance Schottky diode gas sensor based on the heterojunction of three-dimensional nanohybrids of reduced graphene oxide-vertical ZnO vanorods on an AIGaN/GaN layer. *ACS Appl. Mater. Interfaces* **2017**, *9*, 30722–30732. [CrossRef]
39. Li, W.; Guo, J.; Cai, L.; Qi, W.; Sun, Y.; Xu, J.; Sun, M.; Zhu, H.; Xiang, L.; Xie, D.; et al. UV light irradiation enhanced gas sensor selectivity of NO_2 and SO_2 using rGO functionalized with hollow SnO_2 nanofibers. *Sens. Actuators B Chem.* **2019**, *290*, 443–452. [CrossRef]
40. Chen, D.; Tang, J.; Zhang, X.; Fang, J.; Li, Y.; Zhuo, R. Detecting decompositions of sulfur hexafluoride using reduced graphene oxide decorated with Pt nanoparticles. *J. Phys. D Appl. Phys.* **2018**, *51*, 185304. [CrossRef]
41. Chen, A.; Liu, R.; Peng, X.; Chen, Q.; Wu, J. 2D hybrid nanomaterials for selective detection of NO_2 and SO_2 using "light on and off" strategy. *ACS Appl. Mater. Interfaces* **2017**, *9*, 37191–37200. [CrossRef] [PubMed]
42. Tyagi, P.; Sharma, A.; Tomar, M.; Gupta, V. A comparative study of RGO-SnO_2 and MWCNT-SnO_2 nanocomposites based SO_2 gas sensors. *Sens. Actuators B Chem.* **2017**, *248*, 980–986. [CrossRef]
43. Chaudhary, V.; Kaur, A. Enhanced room temperature sulfur dioxide sensing behaviour of in situ polymerized polyaniline–tungsten oxide nanocomposite possessing honeycomb morphology. *RSC Adv.* **2015**, *5*, 73535–73544. [CrossRef]
44. Stankova, M.; Vilanova, X.; Calderer, J. Detection of SO_2 and H_2S in CO_2 stream by means of WO_3-based micro-hotplate sensors. *Sens. Actuators B Chem.* **2004**, *2*, 219–225. [CrossRef]
45. Ghimbeu, M.; Lumbreras, M.; Schoonman, J. Electrosprayed metal oxide semiconductor films for sensitive and selective detection of hydrogen sulfide. *Sensors* **2009**, *9*, 9122–9132. [CrossRef] [PubMed]
46. Shen, F.; Wang, D.; Liu, R. Edge-tailored graphene oxide nanosheet-based field effect transistors for fast and reversible electronic detection of sulfur dioxide. *Nanoscale* **2012**, *5*, 537–540. [CrossRef] [PubMed]
47. Zhang, D.; Liu, J.; Jiang, C.; Li, P.; Sun, Y. High-performance sulfur dioxide sensing properties of layer-by-layer self-assembled titania-modified graphene hybrid nanocomposite. *Sens. Actuators B Chem.* **2017**, *245*, 560–567. [CrossRef]
48. Tyagi, P.; Sharma, A.; Tomar, M.; Gupta, V. Metal oxide catalyst assisted SnO_2 thin film based SO_2 gas sensor. *Sens. Actuators B Chem.* **2016**, *224*, 282–289. [CrossRef]
49. Zhang, X.; Tie, J.; Zhang, J. A Pt-doped TiO_2 nanotube arrays sensor for detecting SF_6 decomposition products. *Sensors* **2013**, *13*, 14764–14776. [CrossRef]
50. Chaudhary, V.; Kaur, A. Solitary surfactant assisted morphology dependent chemiresistive polyanilne sensors for room temperature monitoring of low ppm sulphur dioxide. *Polym. Int.* **2015**, *64*, 1475–1481. [CrossRef]
51. Lupan, O.; Chow, L.; Chai, G. A single ZnO tetrapod-based sensor. *Sens. Actuators B Chem.* **2009**, *141*, 511–517. [CrossRef]
52. Zhang, D.; Wu, J.; Peng, L. Room-temperature SO_2 gas-sensing properties based on a metal-doped MoS_2 nanoflower: An experimental and density functional theory investigation. *J. Mater. Chem. A* **2017**, *5*, 20666–20677. [CrossRef]
53. Das, S.; Chakraborty, S.; Parkash, O. Vanadium doped tin dioxide as a novel sulfur dioxide sensor. *Talanta* **2008**, *75*, 385–389. [CrossRef] [PubMed]
54. Morris, D.; Egdell, R. Application of V-doped TiO_2 as a sensor for detection of SO_2. *J. Mater. Chem.* **2001**, *11*, 3207–3210. [CrossRef]

55. Kumar, R.; Avasthi, D.; Kaur, A. Fabrication of chemiresistive gas sensors based on multistep reduced graphene oxide for low parts per million monitoring of sulfur dioxide at room temperature. *Sens. Actuators B Chem.* **2017**, *242*, 461–468. [CrossRef]
56. Nisar, J.; Topalian, Z.; de Sarkar, A.; Osterlund, L.; Ahuja, R. TiO_2 based gas sensor: A possible application to SO_2. *ACS Appl. Mater. Interfaces* **2013**, *5*, 8516–8522. [CrossRef]
57. Zhang, S.; Song, P.; Liu, L.; Yang, Z.; Wang, Q. In_2O_3 nanosheets array directly grown on Al_2O_3 ceramic tube and their gas sensing performance. *Ceram. Int.* **2017**, *43*, 7942–7947. [CrossRef]
58. Si, W.; Du, W.; Wang, F.; Wu, L.; Liu, J.; Liu, W.; Cui, P.; Zhang, X. One-pot hydrothermal synthesis of nano-sheet assembled NiO/ZnO microspheres for efficient sulfur dioxide detection. *Ceram. Int.* **2020**, *46*, 7279–7287. [CrossRef]
59. Zhuo, Q.; Zeng, W.; Chen, W.; Xu, L.; Kumar, R.; Umar, A. High sensitive and low-concentration sulfur dioxide (SO_2) gas sensor application of heterostructure NiO-ZnO nanodisks. *Sens. Actuators B Chem.* **2019**, *298*, 126870. [CrossRef]
60. Ye, H.; Liu, L.; Xu, Y.; Wang, L.; Chen, X.; Zhang, K.; Liu, Y.; Koh, S.; Zhang, G. SnSe monolayer: A promising candidate of SO_2 sensor with high adsorption quantity. *Appl. Surf. Sci.* **2019**, *484*, 33–38. [CrossRef]
61. Seif, A.; nikfarjam, A.; Ghassem, H. UV enhanced ammonia gas sensing properties of PANI/TiO_2 core-shell nanofibers. *Sens. Actuators B Chem.* **2019**, *298*, 126906.
62. Bai, J.; Zhao, C.; Gong, H.; Wang, Q.; Huang, B.; Sun, G.; Wang, Y.; Zhou, J.; Xie, E.; Wang, F. Debye-length controlled gas sensing performances in NiO@ZnO p-n junctional core-shell nanotubes. *J. Phys. D Appl. Phys.* **2019**, *52*, 285103. [CrossRef]
63. Su, P.; Zheng, Y. Room-temperature ppb-level SO_2 gas sensors based on RGO/WO_3 and MWCNTs/WO_3 nanocomposites. *Anal. Methods* **2021**, *13*, 782–788. [CrossRef] [PubMed]
64. Veeralingam, S.; Sahatiya, P.; Badhulika, S. Low cost, flexible and disposable $SnSe_2$ based photoresponsive ammonia sensor for detection of ammonia in urine samples. *Sens. Actuators B Chem.* **2019**, *297*, 126725. [CrossRef]
65. Yang, Z.; Zhang, D.; Wang, D. Carbon monoxide gas sensing properties of metal-organic frameworks-derived tin dioxide nanoparticles/molybdenum diselenide nanoflowers. *Sens. Actuators B Chem.* **2020**, *304*, 127369. [CrossRef]
66. Guo, J.; Li, Y.; Jiang, B.; Gao, H.; Wang, T.; Sun, P.; Liu, F.; Yan, X.; Liang, X.; Gao, Y.; et al. Xylene gas sensing properties of hydrothermal synthesized SnO_2-Co_3O_4 microstructure. *Sens. Actuators B Chem.* **2020**, *310*, 127780. [CrossRef]
67. Beniwai, A.; Sunny. Electrospun SnO_2/PPy nanocomposite for ultra-low ammonia concentration detection at room temperature. *Sens. Actuators B Chem.* **2019**, *296*, 126660. [CrossRef]
68. Xue, Q.; Chen, H.; Li, Q.; Yan, K.; Besenbacher, F.; Dong, M. Room-temperature high-sensitivity detection of ammonia gas using the capacitance of carbon/silicon heterojunctions. *Energy Environ. Sci.* **2010**, *3*, 288–291. [CrossRef]